Small-signal admittance electrolyser circuit model for stability studies of multi-energy DC grid-connected hydrogen systems

Oriol Cartiel, Juan-José Mesas, Pablo Horrillo-Quintero, Pablo García Triviño, Raúl Sarrias Mena, Luis Sainz, Luis M. Fernández-Ramírez

Published in:
International Journal of Hydrogen Energy

DOI (link to publication from Publisher):
https://doi.org/10.1016/j.ijepes.2025.110899

Publication date:
17 July 2025

Document Version:
Accepted version

Electrical Power and Energy Systems 170 (2025) 110899

Contents lists available at ScienceDirect

International Journal of Electrical Power and Energy Systems

journal homepage: www.elsevier.com/locate/ijepes

Small-signal admittance electrolyser circuit model for stability studies of multi-energy DC grid-connected hydrogen systems

Oriol Cartiel [a,*], Juan-José Mesas [b], Pablo Horrillo-Quintero [c], Pablo García-Triviño [c], Raúl Sarrias-Mena [d], Luis Sainz [a], Luis M. Fernández-Ramírez [c]

[a] Department of Electrical Engineering (DEE), Escola Tècnica Superior d'Enginyeria Industrial de Barcelona (ETSEIB), Universitat Politècnica de Catalunya - BarcelonaTech (UPC), Av. Diagonal 647, 08028 Barcelona, Spain
[b] Department of Electrical Engineering (DEE), Escola d'Enginyeria de Barcelona Est (EEBE), Universitat Politècnica de Catalunya - BarcelonaTech (UPC), Av. d'Eduard Maristany 16, 08019 Barcelona, Spain
[c] Research Group in Sustainable and Renewable Electrical Technologies – SURET (PAIDI-TEP-023), Department of Electrical Engineering, ETSIA, University of Cádiz, Avda. Ramón Puyol, s/n., 11202 Algeciras, Spain
[d] Research Group in Sustainable and Renewable Electrical Technologies – SURET (PAIDI-TEP-023), Department of Engineering in Automation, Electronics and Computer Architecture & Networks, ETSIA, University of Cádiz, Avda. Ramón Puyol, s/n., 11202 Algeciras, Spain

ARTICLE INFO

Keywords:
Electrolyser
Hydrogen storage systems
Multi-energy DC grids
Positive-mode-damping stability criterion
Small-signal admittance-based model

ABSTRACT

Renewable energies are increasingly being used as net-zero carbon power suppliers, replacing fossil fuels. Simultaneously, energy storage systems are emerging as complementary solutions to the intermittent and uncertain nature of these energies. In particular, hydrogen storage systems are being noticed as a promising option for future multi-energy DC power systems. One of the primary research topics regarding hydrogen storage systems is the prediction of system instabilities caused by interactions between DC grids and electrolyser and fuel cell DC/DC converters when hydrogen storage systems are connected. Frequency-domain methods are the most suitable to assess stability in large multi-energy DC power systems. Notably, the positive-mode-damping stability criterion is a friendly frequency-domain method that offers several benefits over techniques such as the generalised Nyquist criterion. The present paper contributes a small-signal admittance-based model of the electrolyser circuit of hydrogen storage systems. Using the proposed model, it analyses the resonance and the damping frequency regions of electrolyser circuits of hydrogen storage systems, and studies the influence of electrolyser circuit and multi-energy DC grid parameters on oscillatory instabilities by the positive-mode-damping stability criterion. The model and stability results are validated using MATLAB/Simulink time-domain and OPAL-RT (OPAL-RT4512) real-time simulations.

1. Introduction

Renewable energies (mainly wind and photovoltaic energy sources) are increasingly being used worldwide as green, net-zero carbon power suppliers, replacing fossil fuel power generation [1]. However, these energies have several drawbacks, such as their intermittent and uncertain nature [2], diverse time scales, large power range variations and different dynamic behaviour compared to consumption [3]. This makes it hard to dynamically align their performance with load characteristics [4]. To address these issues, capacity-oriented (e.g., pumped storage hydropower or hydrogen) [5] and access-oriented (e.g., batteries, flywheels or supercapacitors) energy storage systems are globally emerging as interesting solutions [6]. Among all of these solutions, Hydrogen Storage Systems (HSSs) are becoming an attractive option as multi-energy DC conversion hubs in forthcoming multi-energy power systems worldwide [3,5]. Hydrogen is one of the cleanest, and most promising and efficient energy carriers with large energy density, high capacity, long lifespan, and easy storage possibilities [7,8]. On the other hand, it is also a long-term, steady-state energy storage system with slow dynamics, which must be integrated with batteries or supercapacitors to meet transient energy demands [3,4]. As a result, the study of HSSs has become one of the most prominent topics [1,3], attracting significant international attention in multi-energy power system research areas such as wind power plant systems [9,10], photovoltaic energy systems [11], stand-alone renewable energy systems [8], microgrids [12], and gas-to-power systems [13].

* Corresponding author.
E-mail address: oriol.cartiel@upc.edu (O. Cartiel).

https://doi.org/10.1016/j.ijepes.2025.110899
Received 25 December 2024; Received in revised form 25 April 2025; Accepted 8 July 2025
Available online 17 July 2025

In multi-energy DC systems, the HSS works as an energy conversion hub consisting of an electrolyser (EZ), hydrogen storage tank (HT), and fuel cell (FC) connected at the point of common coupling (PCC) of the DC grid (see Fig. 1) [1]. These three components of the HSS are utilised for hydrogen production, storage, and consumption, respectively. That is, the EZ absorbs the excess of DC grid power and produces hydrogen, which is then stored in the HT, while the FC uses the hydrogen from the HT to compensate for the lack of DC grid power [14]. As can be seen in Fig. 1, the DC grid and the EZ/FC are interfaced by DC/DC buck/boost converters [8,14], respectively, to operate under different voltage and power characteristics [4]. Moreover, a control system is applied to drive the duty cycle of the converter switches and regulate the DC grid active power to the EZ via the DC/DC buck converter (i.e., from the DC grid to the HSS EZ system), and the FC active power to the DC grid via the boost DC converter (i.e., from the HSS FC system to the DC grid) [8,14]. The use of DC/DC buck and boost converters facilitates efficient and reliable integration of HSSs into renewable energy systems. However, it also presents challenges such as large- and small-signal power system instabilities. Large-signal stabilities are concerned with the system's behaviour under larger disturbances, while small-signal stabilities focus on the system's ability to return to a steady state after a small disturbance [15,16]. In particular, small-signal instabilities caused by the interaction between DC grids and HSS converters and their control [15,16] are attracting increasing interest from electric utilities, power electronics manufacturers, and researchers due to their potential consequences [17]. The interaction of the HSS with the DC grid can be decoupled into interactions of the HSS EZ and HSS FC systems with the DC grid because of the slow dynamics of the HSS [3,4]. This allows the separate assessment of HSS EZ and HSS FC system stabilities. Small-signal stabilities in power electronics-based systems can be investigated using various approaches, which are typically divided into time-domain eigenvalue analysis [15,18] and frequency-domain methods [19]. Time-domain eigenvalue analysis has several important drawbacks because detailed information is required for all system elements and high-order dynamic equations must be developed. On the other hand, frequency-domain methods are powerful tools for stability studies due to their ability to characterise system stability from black-box models and their lower computational effort [19]. In particular, the impedance-based stability criterion [20,21] and the passivity-based stability criterion [22] are an extensively applied frequency-domain approach for assessing stability in DC and AC power electronics-based systems [20,23]. According to this criterion, the impedance ratio (or minor loop gain) of the source and load must satisfy the Bode plot or the Nyquist diagram criteria for the power electronics-based system to be stable [24,25]. However, it is well documented that the impedance-based stability criterion is a local stability approach which cannot be readily applied in multi-terminal power electronics-based systems because it can provide inaccurate stability conclusions when several power electronics are connected [26]. To address this problem, stability is commonly evaluated by applying the generalised Nyquist criterion (GNC) to the nodal admittance matrix, which extends the Nyquist criterion to Multiple-Input Multiple-Output systems [19]. However, GNC has several drawbacks [27]: (i) it requires significant computational effort to evaluate unstable poles in the right half-plane for large-scale nodal admittance matrices [28,29]; (ii) it may yield incorrect stability results due to misleading associations when deriving the closed-loop transfer function [26,30]; and (iii) it is challenging to interpret due to the numerous Nyquist plots associated with the eigenvalues [31]. The recently proposed positive-mode-damping (PMD) stability criterion offers a straightforward, practical alternative for assessing stability in power electronics-based systems [27], overcoming GNC's limitations. Based on resonance mode analysis (RMA) [32,33], the PMD stability criterion enables a more effective examination of instabilities than both the impedance-based stability criterion and GNC. Additionally, it facilitates sensitivity studies using participation factors (PFs), supports black-box models [31], and provides damping margin indicators [34].

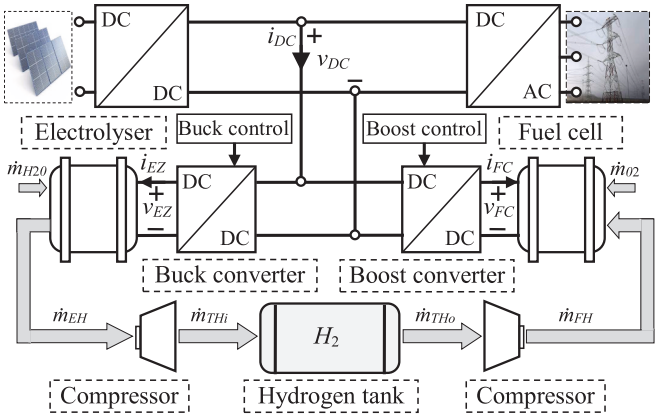

Fig. 1. DC grid-connected hydrogen storage system.

Small-signal averaging modelling of DC/DC buck and boost converters for control design has been extensively researched. A comprehensive study on DC/DC converter modelling is presented in [35,36]. Averaging and linearisation techniques for DC/DC buck converter modelling, along with the analysis of the converter closed-loop transfer function for control design, are shown in [37]. Comprehensive modelling [38], simulation, and computational implementation of DC/DC buck converters (and other DC/DC converters) are developed in [39,40]. Moreover, small-signal models of DC/DC buck and boost converters are applied for stability studies under particular operational conditions. Closed-loop *s*-domain modelling of DC/DC boost converters is studied in [41] to explore their stability capabilities. Stability between load and source DC/DC buck converters, where tightly regulated load converters show a constant power characteristic, is analysed in [42]. This regulation can lead to negative impedance instability in the feeder converter, resulting in increased interest in the stability analysis of converters feeding constant power such as in case of generic DC/DC power converters [43], DC/DC boost converters [44,45] and cascade converters [46]. A stability analysis of voltage-controlled DC/DC buck converters supplied from a periodic source, which may be a common situation in renewable energy applications, is conducted in [47]. Stability of DC/DC buck converters under variations in system load, line resistance, operating temperature, and uncertainties in the system model is addressed in [48]. However, to the best of the authors' knowledge, the impact of HSS on DC grid stability due to the interaction of DC/DC buck and boost converters has not yet been studied in detail.

The original contributions of the paper are as follows: (i) a small-signal admittance-based model of HSS EZ circuits for stability studies, and (ii) its application for frequency-domain stability assessment of multi-energy DC grid-connected HSS systems. The small-signal admittance-based model is precisely obtained from the small-signal state-space average model of the DC/DC buck converter, considering all the main components and controls. The paper analyses the resonances and damping regions of the HSS EZ circuit across both synchronous and harmonic frequency ranges. Additionally, it presents a comprehensive overview of the influence of HSS EZ circuit and DC grid parameters on them. The dynamic behaviour stability of a DC grid is examined by the PMD stability criterion to illustrate the previous studies and potential causes of instability in DC grid-connected HSS EZ circuits. The model and results are validated by both MATLAB/Simulink and OPAL-RT4512 hardware-in-the-loop (HIL) simulations, ensuring its efficacy under realistic operational conditions [49].

2. Admittance model of the HSS EZ circuit

The HSS EZ circuit in Fig. 2 produces hydrogen from the DC grid current, which is then stored in the HT. The EZ is fed from the DC grid via the DC/DC buck converter, and the hydrogen production $\dot{m}_{EH}$ is

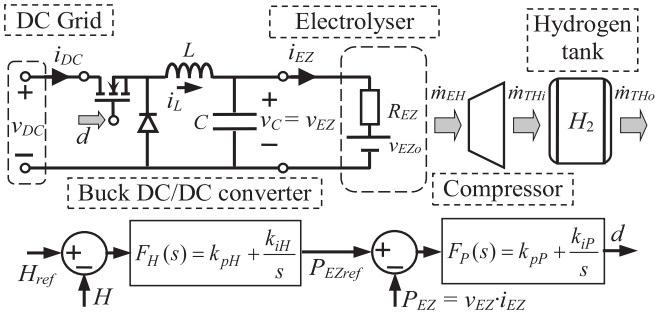

Fig. 2. HSS EZ circuit.

generated from the EZ consumed DC current i_{EZ}. Subsequently, the hydrogen pressure is increased in the compressor to obtain the final hydrogen production $\dot{m}_{THi}$, which is stored in the HT. There is also the hydrogen consumption $\dot{m}_{THo}$ from the HT to the FC, which is not considered in the HSS EZ circuit modelling. The EZ hydrogen production is controlled with the duty cycle d of the DC/DC buck converter, which is generated through the reference value of the EZ input active power P_{EZref} imposed to the inner converter PI control. This reference value is, in turn, derived from the reference level of the hydrogen in the HT H_{ref} imposed to the outer converter PI control. As an example of HSS EZ circuit operation, simulations using MATLAB/Simulink models of the HSS EZ circuit in Fig. 2 supplied by an ideal DC grid and the data in Table 1 are illustrated in Fig. 3 by plotting the variables d, P_{EZ}, $\dot{m}_{THi}$ and H. An initial state with the hydrogen tank empty ($H = 0$ pu) is assumed and H_{ref} is set to 1 pu at 1 s to fill the tank completely. At the beginning of the simulation (left plots in Fig. 3), the four previous variables respond appropriately to the setpoints according to their respective time constants. Since the process of filling the tank is slow due to the low mass flow of hydrogen supplied by the EZ, the simulation is split, with the final stage shown by the plots on the right side of Fig. 3. In this final part, the tank approaches full capacity (H is close to 1 pu), and the control system adjusts the power and, consequently, the mass flow to match the control setpoint for H. The fair accuracy of the HSS EZ control models is validated by the dynamic responses of the MATLAB/Simulink simulations.

The small-signal transfer function of the DC cable, the DC/DC buck converter, and the EZ is derived from its state-space equations. This transfer function is then combined with the small-signal transfer functions of the converter PI controls, the EZ, the compressor, and the HT to obtain the small-signal admittance-based model of the HSS EZ circuit.

2.1. DC/DC buck converter modelling

The study of the DC/DC buck converter (see Fig. 4) is only briefly described in this subsection as it is well-documented in the literature (see Introduction). The converter is supplied through the DC cable (characterised as a resistor r) and loaded with the EZ, whose equivalent circuit is characterised by the series resistor R_{EZ} and the open-circuit voltage source v_{EZo} (see Subsection 2.2). The converter works in the well-known "*on*" and "*off*" states, defined by the duty cycle d over one switching cycle T (see Fig. 4) [37,39]. This duty cycle, defined as the ratio between the *on*-time period T_{on} and the switching cycle T, allows the converter output voltage (i.e., the EZ input voltage v_{EZ}) to be adjusted, and the EZ input active power P_{EZref} or the EZ input current i_{EZref} to be controlled to track the hydrogen production $\dot{m}_{EH}$.

Table 1
1100 V 500 kW HSS EZ circuit parameters.

$r = 1$ mΩ	$V_{EZo} = 590$ V	$\tau_C = 0.75$ s	$k_{pH} = 500$ MW
$L = 0.201$ mH	$R_{EZ,c} = 2$ mΩ/cell	$Q_T = 25$ kg of H_2	$k_{iH} = 10$ MW·s^{-1}
$C = 1.25$ mF	$N°\ cells = 400$	$k_{iP} = 10^{-4}$ (W·s)$^{-1}$	$k_{pP} = 10^{-6}$ W^{-1}

As can be observed in Fig. 4, the state-space equations of the DC/DC buck converter, together with the DC cable and the EZ equivalent circuit over the "*on*" and "*off*" periods of the converter, are [37,39]

$$\begin{aligned}
\frac{d}{dt}\underbrace{\begin{bmatrix} i_L \\ v_C \end{bmatrix}}_{\mathbf{x}} &= \underbrace{\begin{bmatrix} -\frac{r}{L} & -\frac{1}{L} \\ \frac{1}{C} & -\frac{1}{R_{EZ}C} \end{bmatrix}}_{\mathbf{A_{on}}} \begin{bmatrix} i_L \\ v_C \end{bmatrix} + \underbrace{\begin{bmatrix} \frac{1}{L} & 0 \\ 0 & \frac{1}{R_{EZ}C} \end{bmatrix}}_{\mathbf{B_{on}}} \underbrace{\begin{bmatrix} v_{DC} \\ v_{EZo} \end{bmatrix}}_{\mathbf{u}} \\
\underbrace{\begin{bmatrix} i_{DC} \\ i_{EZ} \end{bmatrix}}_{\mathbf{y}} &= \underbrace{\begin{bmatrix} 1 & 0 \\ 0 & \frac{1}{R_{EZ}} \end{bmatrix}}_{\mathbf{C_{on}}} \begin{bmatrix} i_L \\ v_C \end{bmatrix} + \underbrace{\begin{bmatrix} 0 & 0 \\ 0 & -\frac{1}{R_{EZ}} \end{bmatrix}}_{\mathbf{E_{on}}} \begin{bmatrix} v_{DC} \\ v_{EZo} \end{bmatrix},
\end{aligned} \tag{1}$$

$$\begin{aligned}
\frac{d}{dt}\begin{bmatrix} i_L \\ v_C \end{bmatrix} &= \underbrace{\begin{bmatrix} 0 & -\frac{1}{L} \\ \frac{1}{C} & -\frac{1}{R_{EZ}C} \end{bmatrix}}_{\mathbf{A_{off}}} \begin{bmatrix} i_{L1} \\ v_{C1} \end{bmatrix} + \underbrace{\begin{bmatrix} 0 & 0 \\ 0 & \frac{1}{R_{EZ}C} \end{bmatrix}}_{\mathbf{B_{off}}} \begin{bmatrix} v_{DC} \\ v_{EZo} \end{bmatrix} \\
\begin{bmatrix} i_{DC} \\ i_{EZ} \end{bmatrix} &= \underbrace{\begin{bmatrix} 0 & 0 \\ 0 & \frac{1}{R_{EZ}} \end{bmatrix}}_{\mathbf{C_{off}}} \begin{bmatrix} i_L \\ v_C \end{bmatrix} + \underbrace{\begin{bmatrix} 0 & 0 \\ 0 & -\frac{1}{R_{EZ}} \end{bmatrix}}_{\mathbf{E_{off}}} \begin{bmatrix} v_{DC} \\ v_{EZo} \end{bmatrix},
\end{aligned} \tag{2}$$

where L and C are the converter inductor and capacitor, respectively, $\mathbf{x} = [i_L\ v_C]^{\mathrm{T}}$ is the state vector (with i_L and v_C being the inductor current and the capacitor voltage), $\mathbf{u} = [v_{DC}\ v_{EZo}]^{\mathrm{T}}$ is the input vector (with v_{DC} and v_{EZo} being the DC grid voltage and EZ open-circuit voltage source), and $\mathbf{y} = [i_{DC}\ i_{EZ}]^{\mathrm{T}}$ is the output vector (with i_{DC} and i_{EZ} being the output DC and input EZ currents).

Using the state-space average method [38,40] the small-signal state-space equations of the DC/DC buck converter, together with the DC cable and the EZ equivalent circuit, are expressed from (1) and (2) as [38,40]

$$\left.\begin{aligned}
\frac{d\mathbf{x}}{dt} &= \big(\mathbf{A_{on}}d + \mathbf{A_{off}}(1-d)\big)\mathbf{x} + \big(\mathbf{B_{on}}d + \mathbf{B_{off}}(1-d)\big)\mathbf{u} \\
\mathbf{y} &= \big(\mathbf{C_{on}}d + \mathbf{C_{off}}(1-d)\big)\mathbf{x} + \big(\mathbf{E_{on}}d + \mathbf{E_{off}}(1-d)\big)\mathbf{u}
\end{aligned}\right\} \Rightarrow$$

$$\left.\begin{aligned}
\frac{d\Delta\mathbf{x}}{dt} &= \mathbf{A}\Delta\mathbf{x} + \mathbf{B}\Delta\mathbf{u} + \overbrace{\big(\big(\mathbf{A_{on}} - \mathbf{A_{off}}\big)\mathbf{x_0} + \big(\mathbf{B_{on}} - \mathbf{B_{off}}\big)\mathbf{u_0}\big)}^{\mathbf{D_x}}\Delta d \\
\Delta\mathbf{y} &= \mathbf{C}\Delta\mathbf{x} + \mathbf{E}\Delta\mathbf{u} + \underbrace{\big(\big(\mathbf{C_{on}} - \mathbf{C_{off}}\big)\mathbf{x_0} + \big(\mathbf{E_{on}} - \mathbf{E_{off}}\big)\mathbf{u_0}\big)}_{\mathbf{D_y}}\Delta d
\end{aligned}\right\} \tag{3}$$

$$\mathbf{M} = \mathbf{M_{on}}d_0 + \mathbf{M_{off}}(1-d_0) \quad (\mathbf{M} = \mathbf{A},\ \mathbf{B},\ \mathbf{C},\ \mathbf{E}),$$

where

$$\begin{aligned}
\boldsymbol{A} &= \begin{bmatrix} -\frac{r}{L}d_0 & -\frac{1}{L} \\ \frac{1}{C} & -\frac{1}{R_{EZ}C} \end{bmatrix} \quad \boldsymbol{B} = \begin{bmatrix} \frac{d_0}{L} & 0 \\ 0 & \frac{1}{R_{EZ}C} \end{bmatrix} \\
\mathbf{C} &= \begin{bmatrix} d_0 & 0 \\ 0 & \frac{1}{R_{EZ}} \end{bmatrix} \quad \mathbf{E} = \begin{bmatrix} 0 & 0 \\ 0 & -\frac{1}{R_{EZ}} \end{bmatrix} \\
\mathbf{D_x} &= \begin{bmatrix} -\frac{r}{L}i_{L0} + \frac{v_{DC0}}{L} \\ 0 \end{bmatrix}, \quad \mathbf{D_y} = \begin{bmatrix} i_{L0} \\ 0 \end{bmatrix},
\end{aligned} \tag{4}$$

and v_{DC0}, i_{L0}, and d_0 are the steady-state values of the DC grid voltage, converter inductor current, and duty cycle.

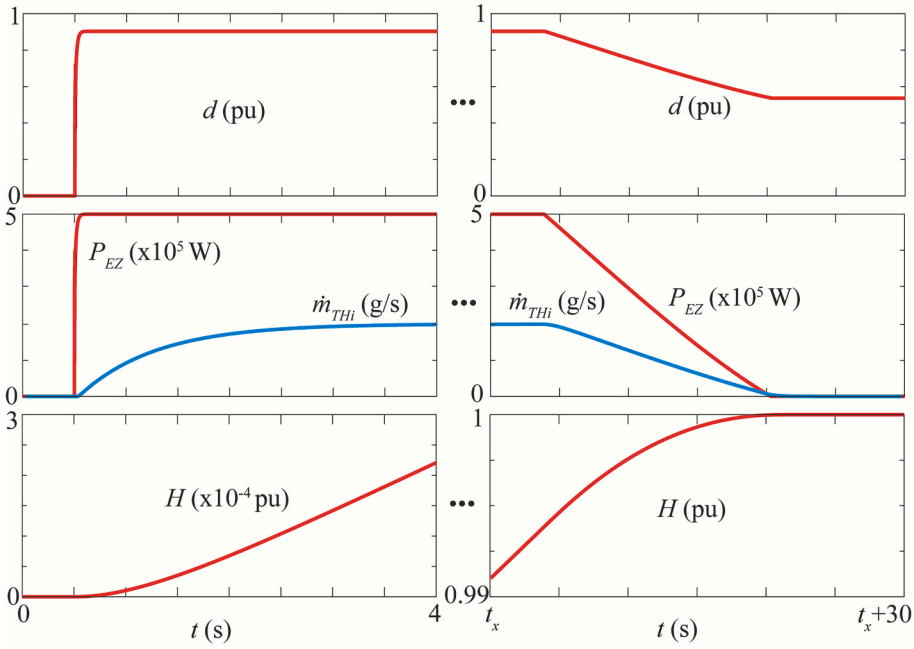

Fig. 3. MATLAB/Simulink simulations of the HSS EZ circuit operation.

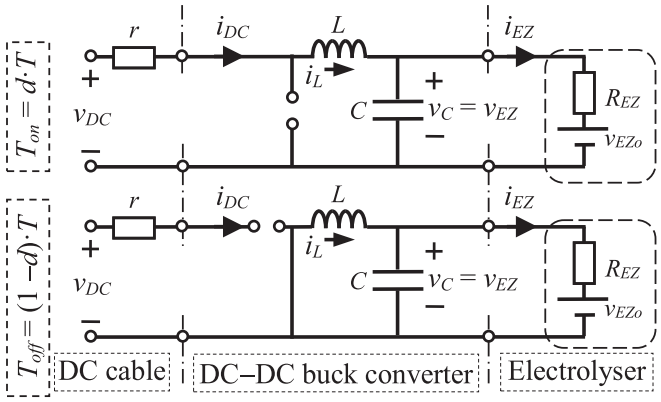

Fig. 4. DC/DC buck converter states.

The small-signal transfer function of the DC cable, DC/DC buck converter, and the EZ is derived from (3) as

$$\Delta\mathbf{y} = \left(\mathbf{C}(s\mathbf{I}-\mathbf{A})^{-1}\mathbf{B}+\mathbf{E}\right)\Delta\mathbf{u} + \left(\mathbf{C}(s\mathbf{I}-\mathbf{A})^{-1}\mathbf{D}_{\mathbf{x}}+\mathbf{D}_{\mathbf{y}}\right)\Delta d$$
$$\Rightarrow \begin{bmatrix}\Delta i_{DC}\\ \Delta i_{EZ}\end{bmatrix} = \begin{bmatrix}Y_{11}(s) & Y_{12}(s)\\ Y_{21}(s) & Y_{22}(s)\end{bmatrix}\begin{bmatrix}\Delta v_{DC}\\ \Delta v_{EZo}\end{bmatrix} + \begin{bmatrix}J_{11}(s)\\ J_{12}(s)\end{bmatrix}\Delta d, \tag{5}$$

where Δv_{EZo} is equal to zero because the EZ open-circuit voltage source v_{EZo} is assumed to be constant, and

$$Y_{11}(s) = \frac{d_0^2(R_{EZ}Cs+1)}{Z_E(s)} \quad Y_{12}(s) = -\frac{d_0}{Z_E(s)}$$
$$Y_{21}(s) = \frac{d_0}{Z_E(s)} \quad Y_{22}(s) = \frac{1}{R_{EZ}}\left(\frac{Ls+d_0r}{Z_E(s)}-1\right)$$
$$J_{11}(s) = i_{L0} + \frac{d_0(v_{DC0}-i_{L0}r)(R_{EZ}Cs+1)}{Z_E(s)} \tag{6}$$
$$J_{21}(s) = \frac{v_{DC0}-i_{L0}r}{Z_E(s)}$$
$$Z_E(s) = (R_{EZ}CL)s^2 + (R_{EZ}Cd_0r+L)s + (R_{EZ}+d_0r).$$

2.2. EZ modelling

The EZ study is focused on proton exchange membrane (PEM) EZs, as they are an emerging technology in renewable energies due to their capacity to operate effectively at large current densities and various power levels within seconds [10]. Several models with different degrees of complexity are used for characterising PEM EZ behaviour [10]. The model in the present study only considers the polarisation curve (i.e., the ratio between EZ input voltage v_{EZ} and current i_{EZ}) and the hydrogen production $\dot{m}_{EH}$ (H_2 mol/s) for two main reasons: (i) the model only focuses on the EZ electrical response (EZ internal processes are not analysed in stability studies), and (ii) simplicity is prioritised over characterisation of the effects of pressure and temperature on EZ behaviour [10,11].

For commercial EZ devices, the ratio between EZ input voltage and current can be considered constant for most polarisation curves. Therefore, the PEM EZ input voltage can be expressed as a linear function of the input current, i.e.,

$$v_{EZ} = R_{EZ}i_{EZ} + v_{EZo}, \tag{7}$$

where the series resistance R_{EZ} characterises the direct relationship between the input voltage and current, while the open-circuit voltage source v_{EZo} characterises the voltage at zero current. Both the series resistance and the open-circuit voltage source values are calculated from the PEM EZ polarisation curve. Disregarding the influence of pressure and temperature leads to a loss of accuracy when these conditions are different from those in the reference polarisation curve. However, both parameters can be recalculated using a new polarisation curve under other pressure and temperature conditions. Thus, the proposed model lacks flexibility for variable pressure and temperature but offers valuable simplicity for stability studies.

The hydrogen production $\dot{m}_{EH}$ is calculated using Faraday's law [10,11]. This production is directly proportional to the EZ input current i_{EZ} and the number of series cells n_c divided by twice the Faraday constant F. Moreover, an efficiency factor called Faraday efficiency η_F is applied to account for deviations of the model from ideal performance:

$$\dot{m}_{EH} = \frac{n_c i_{EZ}}{2F}\eta_F, \tag{8}$$

where, assuming constant EZ temperature, Faraday efficiency is commonly determined as [10]

$$\eta_F = 96.5e^{\left(\frac{0.09}{i_{EZ}} - \frac{75.5}{i_{EZ}^2}\right)}. \tag{9}$$

Combining (8) and (9), the small-signal transfer function of the EZ becomes

$$\begin{aligned} \dot{m}_{EH} &= \frac{n_c i_{EZ}}{2F} 96.5e^{\left(\frac{0.09}{i_{EZ}} - \frac{75.5}{i_{EZ}^2}\right)} \quad \Rightarrow \quad \Delta\dot{m}_{EH} = k_E \Delta i_{EZ} \\ k_E &= 96.5\frac{n_c}{2F}\left(1 - \frac{0.09}{i_{EZ0}} + 2\frac{75.5}{i_{EZ0}^2}\right)e^{\left(\frac{0.09}{i_{EZ0}} - \frac{75.5}{i_{EZ0}^2}\right)}, \end{aligned} \tag{10}$$

where i_{EZ0} is the steady state value of the EZ input current.

2.3. DC/DC buck converter PI control modelling

The small-signal transfer function of the converter PI control is derived in this subsection. The converter inner control of the EZ power is studied in Fig. 2, where the EZ power control generates the duty cycle signal d from the EZ input active power P_{EZref}. The reference value P_{EZref} of the EZ input active power is fixed by the outer PI control of the converter from the reference level of the hydrogen in the HT, H_{ref}.

The small-signal transfer function of the EZ power control is

$$\Delta d = -F_P(s)F_H(s)\Delta H - F_P(s)\Delta P_{EZ}, \tag{11}$$

where $F_H(s) = k_{pH} + k_{iH}/s$ (with k_{pH} and k_{iH} being the proportional and integral gains of the PI control for hydrogen level control), and $F_P(s) = k_{pP} + k_{iP}/s$ (with k_{pP} and k_{iP} being the proportional and integral gains of the PI control for EZ power control). Considering that the EZ open-circuit voltage source v_{EZo} remains constant, the small-signal expression of the EZ input active power is

$$P_{EZ} = R_{EZ}i_{EZ}^2 + v_{EZo}i_{EZ} \;\Rightarrow\; \Delta P_{EZ} = 2R_{EZ}i_{EZ0} + v_{EZo}\Delta i_{EZ}. \tag{12}$$

2.4. Compressor modelling

The EZ hydrogen production is injected into a high-pressure gaseous HT using a compressor. For stability studies, this compressor is commonly modelled as a first-order filter [15,32], with its small-signal transfer function expressed as

$$\dot{m}_{THi} = \underbrace{\frac{1}{\tau_C s + 1}}_{F_C(s)}\dot{m}_{EH} \quad \Rightarrow \quad \Delta\dot{m}_{THi} = F_C(s)\Delta\dot{m}_{EH}, \tag{13}$$

where τ_C is the time constant of the compressor.

2.5. HT modelling

The hydrogen balance in the HT can be expressed by the differential equation

$$\frac{dH}{dt} = \frac{1}{Q_T}(\dot{m}_{THi} - \dot{m}_{THo}), \tag{14}$$

where $\dot{m}_{THi}$ and $\dot{m}_{THo}$ are the high-pressure hydrogen production of the EZ and the consumption of the FC, respectively, and Q_T is the capacity of the HT.

According to (14), and considering only the high-pressure hydrogen production of the EZ, the small-signal transfer function of the HT is expressed as

$$\Delta H = \frac{1}{Q_T s}\Delta\dot{m}_{THi}. \tag{15}$$

2.6. Small-signal admittance model of the HSS EZ circuit

The small-signal admittance model of the HSS EZ circuit is obtained from (5), (10), (11), (13), and (15):

$$\begin{aligned} Y_{DC}(s) &= \frac{\Delta i_{DC}}{\Delta v_{DC}} = Y_{11}(s) + Y_{21}(s)\frac{J_{11}(s)}{J_{EZ}(s) - J_{21}(s)} \\ J_{EZ}(s) &= -\frac{1}{F_P(s)\left(\frac{F_H(s)}{Q_T s}F_C(s)k_E + 2R_{EZ}i_{EZ0} + v_{EZo}\right)}, \end{aligned} \tag{16}$$

where $Y_{11}(s)$, $Y_{21}(s)$, $J_{11}(s)$ and $Y_{21}(s)$ are presented in (6).

3. Multi-energy DC grid stability studies

Multi-energy DC grid stability studies can be addressed by the equivalent circuit in Fig. 5 [20]. This circuit depicts the general schematic with the DC grid, characterised by its nodal admittance matrix $\mathbf{Y_G}(s)$, and the external components connected to the grid nodes. These components (including power electronics-based converters, HSS EZ circuits, and other possible energy vectors) are represented by their equivalent admittance matrix $\mathbf{Y_C}(s) = \mathrm{diag}(Y_{C,1}(s) \ \ldots \ Y_{C,n}(s))$, and the bus current injection vector $\mathbf{I_B}(s) = [I_{B,1}(s) \ \ldots \ I_{B,n}(s)]^{\mathrm{T}}$, where $Y_{C,i}(s) = Y_{H2,i}(s)$ (16) and $I_{B,i}(s) = 0$ for the HSS EZ circuit nodes i. The bus voltage and current relationship at the multi-energy DC grid nodes is expressed by the node voltage method as follows:

$$\left.\begin{aligned} \mathbf{I_G}(s) &= \mathbf{Y_G}(s)\mathbf{V_B}(s) \\ \mathbf{I_G}(s) &= \mathbf{I_B}(s) - \mathbf{Y_C}(s)\mathbf{V_B}(s) \end{aligned}\right\} \Rightarrow$$
$$\mathbf{V_B}(s) = (\mathbf{I} + \mathbf{Z_G}(s)\mathbf{Y_C}(s))^{-1}\mathbf{Z_G}(s)\mathbf{I_B}(s) = \mathbf{Y_B}(s)^{-1}\mathbf{I_B}(s), \tag{17}$$

where $\mathbf{I}$ is the $n \times n$ identity matrix, $\mathbf{Z_G}(s) = \mathbf{Y_G}(s)^{-1}$ is the impedance matrix of the DC grid, and $\mathbf{V_B}(s)$ and $\mathbf{Y_B}(s)$ are the bus voltage vector and nodal admittance matrix of the multi-energy DC grid, respectively.

Instabilities can be studied in the frequency-domain by the GNC if the open-loop matrix transfer function $\mathbf{L}(s) = \mathbf{Z_G}(s)\mathbf{Y_C}(s)$ does not have any right-half-plane pole. This criterion is applied to $\mathbf{L}(s)$ eigenloci, and the system is unstable if the difference between the number of anti-clockwise and clockwise encirclements of the $\mathbf{L}(s)$ eigenvalues around the $(-1, 0)$ point is negative. GNC is challenging for large systems due to the high number of eigenvalues to be analysed. To overcome this drawback, the PMD stability criterion was recently proposed [27,31]. This criterion is a simple approach for stability analysis of large power electronics-based transmission grids. It is based on the eigenvalue decomposition of the nodal admittance matrix $\mathbf{Y_B}(s)$ at each frequency f over the entire frequency range by RMA [32,33]:

$$\mathbf{V_m^{(f)}} = \underbrace{\begin{bmatrix} \lambda_{Y,1}^{(f)} & \cdots & 0 \\ \vdots & \ddots & \vdots \\ 0 & \cdots & \lambda_{Y,n}^{(f)} \end{bmatrix}^{-1}}_{\Lambda_{\mathbf{Y}}^{(f)} = \mathbf{L}^{(f)}\mathbf{Y_B^{(f)}}\mathbf{R}^{(f)}} \mathbf{I_m^{(f)}}, \tag{18}$$

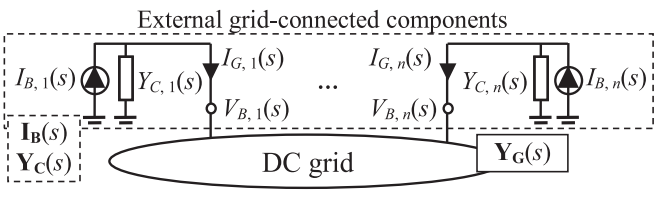

Fig. 5. Schematic of multi-energy DC grids.

where $\mathbf{V_m}^{(f)} = \mathbf{L}^{(f)}\cdot\mathbf{V_B}^{(f)}$ and $\mathbf{I_m}^{(f)} = \mathbf{L}^{(f)}\cdot\mathbf{I_B}^{(f)}$ are the modal voltage and current vectors, $\mathbf{\Lambda_Y}^{(f)}$ is the diagonal eigenvalue matrix of $\mathbf{Y_B}^{(f)}$, and $\mathbf{R}^{(f)}$ and $\mathbf{L}^{(f)} = (\mathbf{R}^{(f)})^{-1}$are the right (in columns) and left (in rows) eigenvector matrices, respectively. The study of peak values of the modal impedances $Z_{m,j}{}^{(f)} = 1/\lambda_{Y,j}{}^{(f)}$ of $(\mathbf{\Lambda_Y}^{(f)})^{-1}$ (with $j = 1, \ldots, n$ being the mode number) at each resonance frequency f_r, which are known as critical resonance modes ($Z_{m,c}{}^{(fr)} = R_{m,c}{}^{(fr)} + jX_{m,c}{}^{(fr)}$), is used to assess stability of power electronics-based transmission grids. The PMD stability criterion states that the grid is stable iff $m_x{\cdot}R_{m,c}{}^{(fr)} > 0$ at resonance frequencies f_r, where m_x is the slope of the imaginary part $X_{m,c}{}^{(fr)}$ of $Z_{m,c}{}^{(fr)}$ and $R_{m,c}{}^{(fr)}$ is the real part of $Z_{m,c}{}^{(fr)}$ (see [27] for details). This stability condition guarantees positive damping of system oscillatory modes, which ensures stable grid conditions.

The PMD stability criterion offers an efficient method for stability assessment, although it has several limitations [27,31]. The primary limitation is that it assumes the condition $|\sigma_k| \ll \omega_k$, where σ_k and ω_k are the real part (related to the system's damping) and the imaginary part (related to the system's oscillation frequency) of the eigenvalues of the system's state-space matrix. This assumption is valid in electrical systems because (i) a power system maintains stable operation for strongly damped modes with large negative σ_k; and (ii) monotonic instability caused by large positive σ_k is less common in power systems. In these cases, growing oscillations due to large positive σ_k are typically curtailed by saturation and nonlinear limiters. Another limitation is that the criterion does not allow for easy calculation of σ_k.

4. Application

In this Section, the HSS EZ circuit model is validated by MATLAB/Simulink and OPAL-RT (see Appendix A for details about the experimental HIL setup) simulations. The behaviour of the HSS EZ is analysed in detail, and a stability study of a DC grid-connected HSS system is presented.

4.1. Validation of the admittance model of the HSS EZ circuit

The small-signal admittance model (16) of the HSS EZ circuit in Fig. 2 is validated in Fig. 6 using the data in Table 1. To achieve this, the frequency response of the small-signal admittance model obtained from the proposed model (16) is compared with MATLAB/Simulink and OPAL-RT (see Appendix A) simulations. The accurate results provided by the model should be highlighted.

4.2. Frequency-domain behaviour of the HSS EZ circuit

The frequency-domain behaviour of the HSS EZ circuit is studied to analyse the factors related to low-damped resonances which could cause oscillatory instabilities in DC grid-connected HSS systems.

The frequency behaviour of the small-signal admittance model of the HSS EZ circuit in Fig. 6 exhibits two important characteristics related to the previously mentioned concern:

- It shows a series resonance frequency (SRF) at 541 Hz. This frequency location can affect the parallel resonance frequencies of DC grid-connected HSS systems, potentially impacting on their oscillatory instabilities.
- It has a negative damping region (NDR) below 27 Hz, which could result in low-damped parallel resonances and sub-synchronous instabilities in DC grid-connected HSS systems.

The numerical study of the influence of the HSS EZ circuit parameters on the above characteristics of the HSS EZ circuit is summarised in Fig. 7. This study shows which parameters contribute to instabilities in DC grid-connected HSS systems and how they could influence these instabilities (see Section 4.3). Based on the results in Fig. 7, it can be concluded that:

- The physical components of the DC/DC buck converter (i.e., the inductor L and the capacitor C) are the most influential parameters on the SRF. Increasing these values results in smaller SRFs. The series resistance R_{EZ} of the EZ also has a significant impact on the SRF, with higher values leading to smaller SRFs.
- The EZ components (i.e., the EZ resistor R_{EZ} and the EZ open-circuit voltage source v_{EZo}), and especially the converter inner control parameters (i.e., the PI control proportional and integral gains of the EZ power control), are the most influential parameters on the NDR.

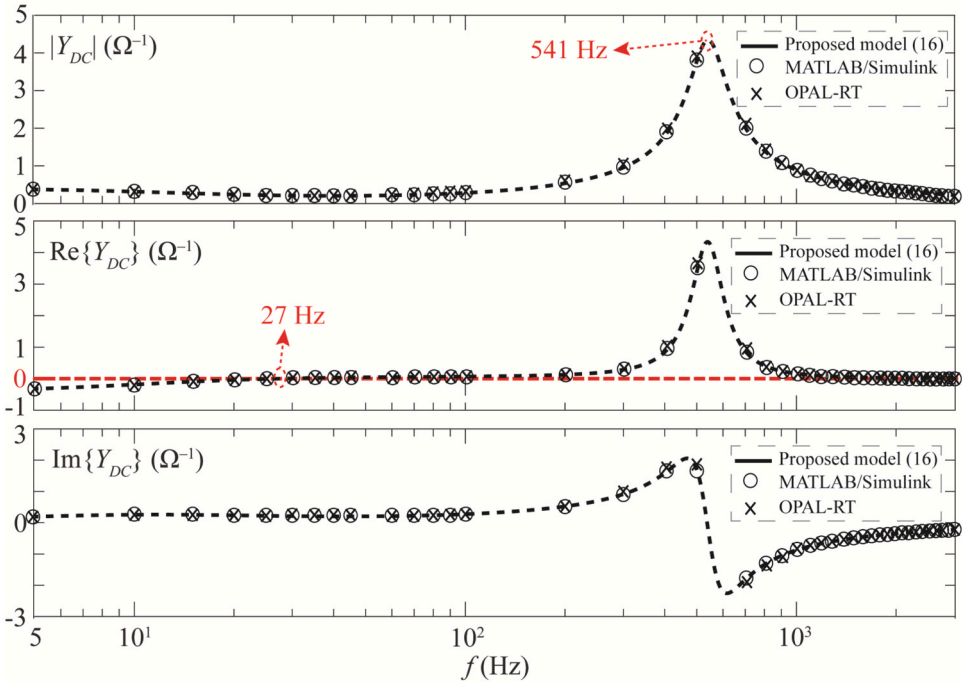

Fig. 6. Validation of the admittance model of the HSS EZ circuit (16) by MATLAB/Simulink and OPAL-RT simulations.

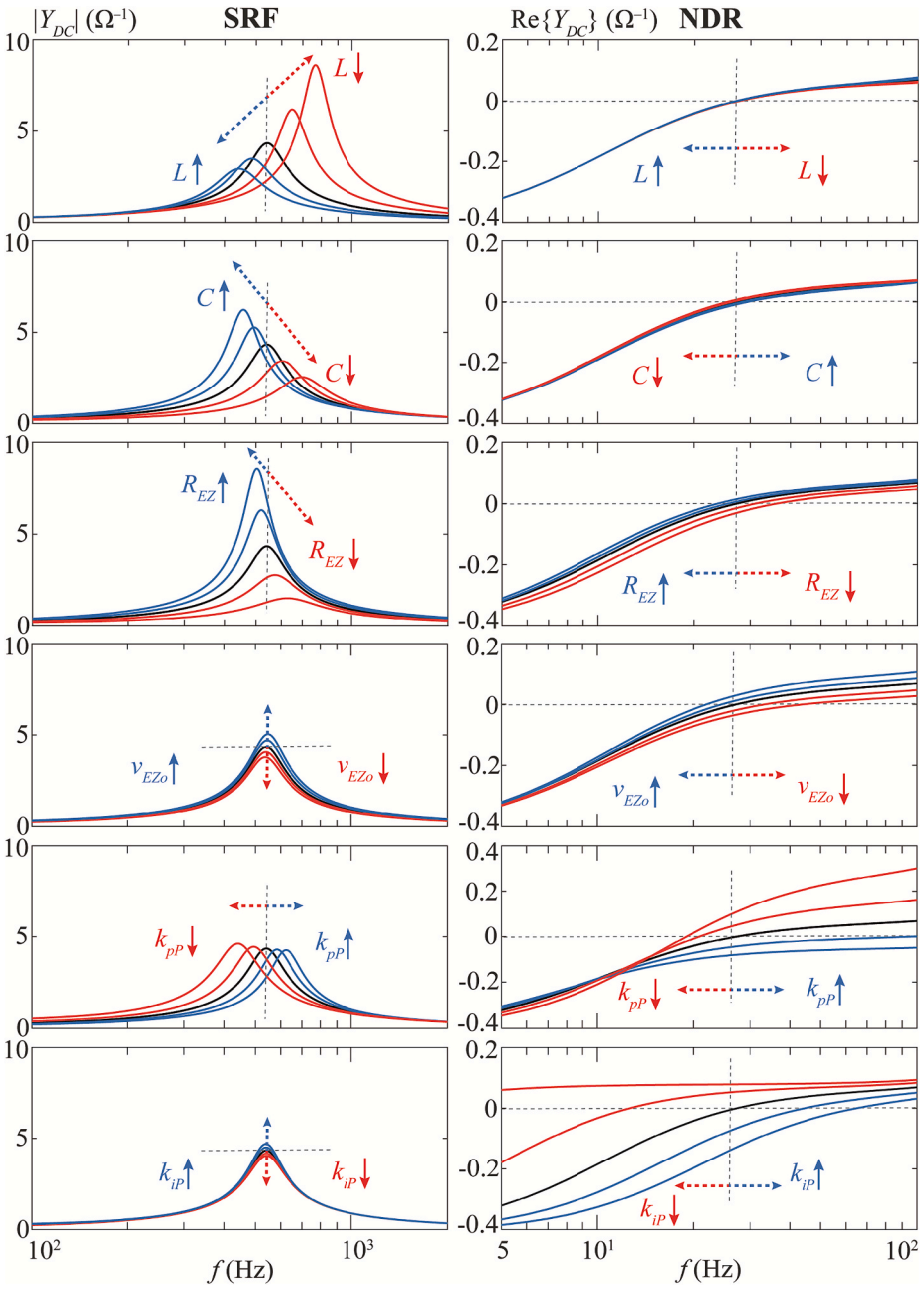

Fig. 7. Impact on the series resonance frequency (left) and negative damping region (right) of the most influential HSS EZ circuit parameters.

Reducing the parameter values of the EZ components results in larger NDRs. Additionally, reducing the parameter values of the converter inner control results in smaller NDRs.

The dynamics of both the compressor and the HT are slow, and their parameters τ_C, k_{pH}, and k_{iH} do not significantly affect the frequency response of the HSS EZ admittance. For this reason, they are omitted from Fig. 7.

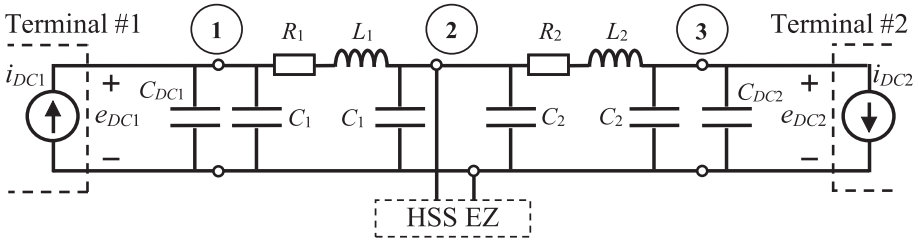

Fig. 8. DC grid with a connected HSS EZ.

4.3. Stability study of the DC grid-connected HSS system

The stability of the two-terminal DC transmission grid with the 3-bus DC grid-connected HSS EZ system in Fig. 8 is studied. Each terminal of the DC grid is represented by an ideal current source that models the active power flow in the grid. Note that the choice of the DC terminal model does not affect the validity of the main conclusions presented below, which were obtained for the system under investigation using the PMD stability criterion. Tables 1 and 2 present data of the HSS EZ system and grid components, respectively. In the initial case (not shown for the sake of space), the DC grid exhibits a resonance at 146 Hz but remains stable. However, any change in the HSS EZ circuit parameters that shifts either the SRF or the NDR to lower or higher frequencies, respectively, could cause instability in the DC grid, as the system resonance could fall within the NDR of the HSS EZ circuit's equivalent admittance. To illustrate this, the control parameter k_{pP} is increased from 1.0×10^{-6} to 1.5×10^{-6} to shift the NDR to higher frequencies (see HSS EZ circuit behaviour in Fig. 7). This adjustment leads to instability in the DC grid, as indicated by the PMD stability criterion results in Fig. 9(a).

Validation is conducted using both MATLAB/Simulink and OPAL-RT (see Appendix A) simulations. In MATLAB/Simulink simulations, the DC grid is constructed and the HSS EZ system of the initial case is connected at the 1-second mark, with k_{pP} changed at the 1.04-second mark (see top of Fig. 9(b)). The simulation shows an oscillation of approximately 168 Hz in the FFT analysis plot (see bottom of Fig. 9(b)), which approximately matches the oscillatory frequency of the instability predicted by the PMD stability criterion (i.e., 171 Hz in Fig. 9(a)). Two separate OPAL-RT simulations are performed due to the limitation of instantaneously modifying k_{pP} in real time. In the first simulation, the HSS EZ system of the initial case is connected at the 1-second mark (see the left figure of Fig. 9(c)), and the system remains stable as expected. In the second simulation, k_{pP} is increased, and upon connecting the HSS EZ system at the 1-second mark, the system begins oscillating and progresses toward instability (see the right figure of Fig. 9(c)). In this second case, an oscillation frequency of approximately 179 Hz is observed in the screenshot of the wave measurement tool (see bottom of the right figure of Fig. 9(c)), which again closely matches the 171 Hz instability frequency predicted by the PMD stability criterion (i.e., 171 Hz in Fig. 9(a)). To ensure compatibility with the OPAL-RT analogue output range, the signals were first expressed in per unit and scaled with a gain of 10. Consequently, a vertical scale of 1.25 V/div is used for both cases in Fig. 9(c). For the horizontal axis, time scales of 500 ms/div and 20 ms/div are applied in the left and right figures of Fig. 9(c), respectively, with voltage base values of 1800 V and 1448 V. It should be mentioned that increasing the value of k_{pP} results in higher power-control-loop bandwidths. According to converter control theory, the bandwidth of a closed-loop system should typically be less than one decade of the DC/DC converter switching frequency, which usually ranges from 100 kHz to 1 MHz. Considering the lowest switching frequency and the HSS EZ circuit parameters in Table 1, the value of k_{pP} is recommended to be less than $1.04{\cdot}10^{-5}$ W^{-1}, which aligns with the k_{pP} values in the study. Moreover, higher values of k_{pP} result in smaller values of the power-control-loop time constant τ_{pP}, potentially compromising system stability due to overly rapid dynamic responses. The dynamic response of P_{EZ} in Fig. 3 was obtained via MATLAB/Simulink simulations for different values of k_{pP} (not shown for brevity). It is observed that increasing k_{pP} leads to sharper responses of P_{EZ} (i.e., smaller τ_{pP}), while decreasing k_{pP} leads to slower dynamics. It is concluded from the numerical simulations that k_{pP} must be less than $5{\cdot}10^{-6}$ W^{-1} to ensure a stable dynamic response of P_{EZ}, which is consistent with the k_{pP} values used in the study.

Additionally, it is worth noting that similar cases of instability can be achieved with each of the parameters studied in Section 4.2 by considering their influence on the SRF or the NDR. For example, the following cases were numerically verified (not shown in detail for the sake of space):

- Adjusting k_{iP} from 1.0×10^{-4} to 4.0×10^{-4} leads to instability in the DC grid due to the NDR shifting toward higher frequencies.
- Adjusting both k_{pP} from 1.0×10^{-6} to 1.1×10^{-6} and k_{iP} from 1.0×10^{-4} to 1.5×10^{-4} (control values that do not destabilise the system independently) while increasing L and C from 0.2 mH to 0.4 mH and from 1.25 mF to 4.25 mF, respectively, leads to instability in the DC grid due to the SRF shifting toward lower frequencies.

Simulation results show that variations in the value of R_{EZ} do not lead to system instability, despite the influence of this parameter on the SRF and NDR (see Fig. 7). This may be because increasing R_{EZ} shifts both the SRF and NDR to lower frequencies, and as a result, the resonance frequencies of the system fall outside the NDR.

Furthermore, similar cases of instability can be observed by considering the influence of passive elements in the DC grid. For instance, increasing both the DC cable inductor L_1 from 3.611 mH to 36.11 mH and the capacitor C_1 from 0.831 μF to 8.31 μF, while adjusting k_{pP} from 1.0×10^{-6} to 1.25×10^{-6} (a range that does not independently destabilise the system), leads to instability due to the resonance frequency shifting to a lower value and entering the NDR of the equivalent admittance. It is also worth noting that DC loads (particularly constant power loads) can impact system stability. These types of loads are known to induce negative impedance instability in DC grids independently of the HSS EZ system connection [42–46].

Table 2
1.1 kV DC grid parameters and values.

$C_{DC1} = 103.1$ mF	$R_1 = 0.104$ Ω	$C_{DC2} = 206.1$ mF	$R_2 = 0.102$ Ω
$C_1 = 0.831$ μF	$L_1 = 3.611$ mH	$C_2 = 4.16$ μF	$L_2 = 13.05$ mH

5. Conclusions

This paper presented a small-signal admittance-based model for the electrolyser circuit of hydrogen storage systems, contributing significantly to the understanding of their stability in multi-energy DC power systems. The model was analytically derived using small-signal state-space averaging techniques and validated by MATLAB/Simulink and OPAL-RT hardware-in-the-loop simulations. These validations demonstrated the model's accuracy and practical utility for predicting dynamic behaviours and potential instabilities in real-world applications. Frequency-domain analysis of the electrolyser circuit of hydrogen storage systems identified two critical stability factors: the series resonance frequency and the negative damping region. The study showed how these factors are influenced by hydrogen storage system circuit parameters, particularly the physical characteristics of the DC/DC buck converter and the electrolyser control gains. It was found that changes in these parameters can cause low-damped resonances and sub-synchronous instabilities when hydrogen storage systems are connected to DC grids. Stability of a DC grid connected to an electrolyser circuit of hydrogen storage systems was assessed using the positive-mode-damping stability criterion. This method proved to be a robust and effective tool for identifying the conditions under which grid resonance could align with the negative damping region, potentially leading to instability. Both numerical and experimental results confirmed the predictions of the positive-mode-damping stability criterion, showcasing its reliability and precision in identifying critical instability frequencies. In addition, the study demonstrated the sensitivity of grid stability to variations in electrolyser parameters of hydrogen storage systems, offering insights into the design and control strategies necessary to mitigate potential instabilities. Specific examples, such as the impact of increasing the proportional and integral gains of the inner control or adjusting the converter's inductor and capacitor values, highlight practical scenarios that could destabilise DC grids. Future research could extend this methodology to include the dynamic

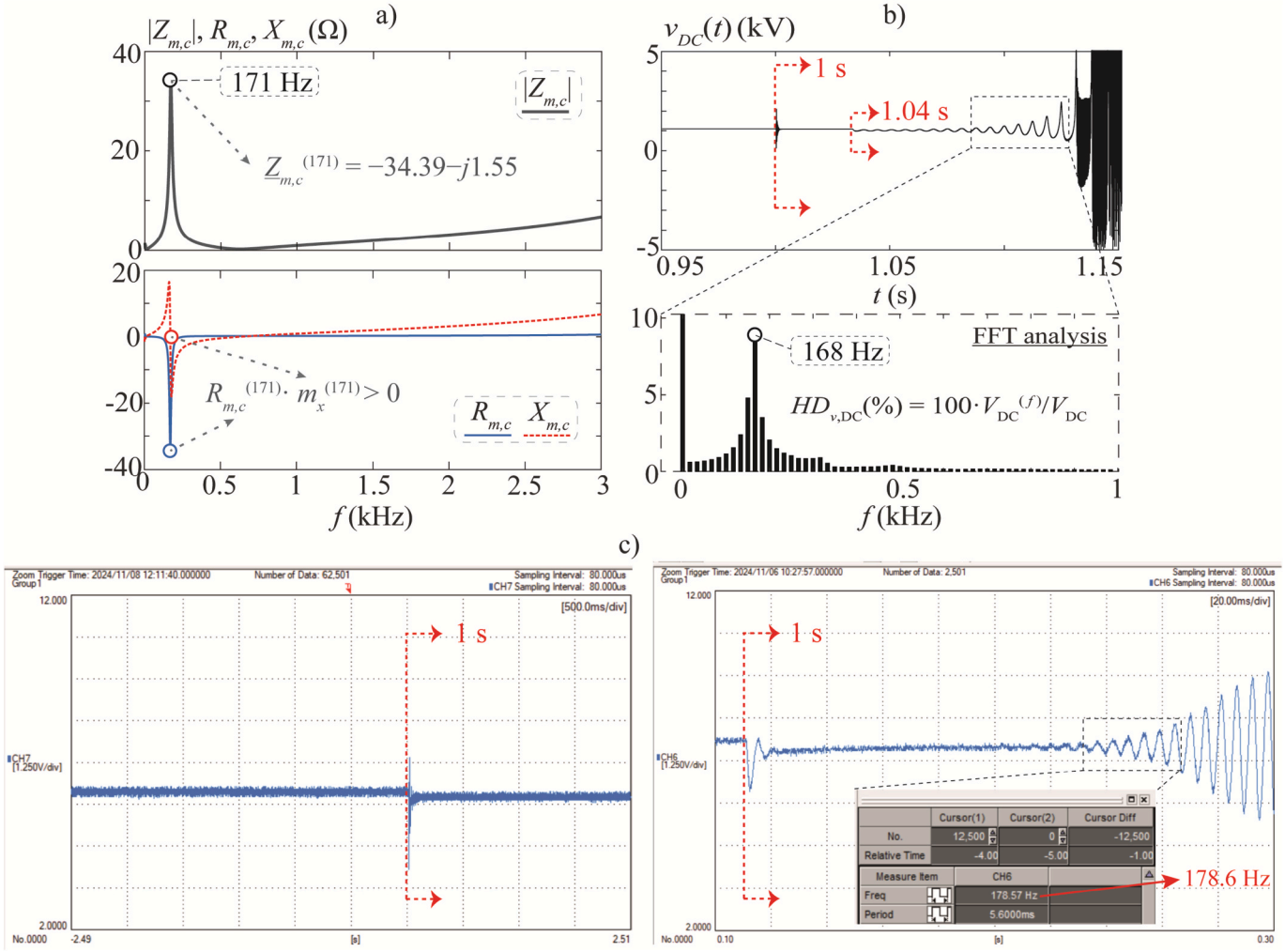

Fig. 9. Stability test results of the DC grid-connected HSS EZ system: a) PMD stability criterion; b) MATLAB/Simulink. c) OPAL-RT.

interaction of fuel cell circuits or investigate the implications of more complex grid topologies and operating conditions. Moreover, factors such as DC/DC converter time delay and measurement errors could be further incorporated into the model of the electrolyser circuit in hydrogen storage systems.

CRediT authorship contribution statement

Oriol Cartiel: Writing – original draft, Visualization, Software, Validation, Investigation, Methodology, Data curation, Formal analysis, Conceptualization. **Juan-José Mesas:** Writing – original draft, Supervision, Investigation, Methodology, Formal analysis, Conceptualization. **Pablo Horrillo-Quintero:** Data curation, Writing – original draft, Validation, Software, Methodology. **Pablo García-Triviño:** Writing – original draft, Validation, Software, Resources, Data curation. **Raúl Sarrias-Mena:** Visualization, Validation, Resources, Software. **Luis Sainz:** Supervision, Funding acquisition, Project administration, Writing – original draft. **Luis M. Fernández-Ramírez:** Supervision, Project administration, Funding acquisition.

Declaration of competing interest

The authors declare that they have no known competing financial interests or personal relationships that could have appeared to influence the work reported in this paper.

Acknowledgements

This work was supported by Ministerio de Ciencia, Innovación y Universidades, Agencia Estatal de Investigación, FEDER, UE (Grants PID2021-123633OB-C32 and PID2021-123633OB-C33 supported by MCIU/AEI/10.13039/501100011033/ FEDER, UE).

Appendix A. Experimental setup

Fig. 10 shows the schematic of the experimental setup constructed in the laboratory for performing real-time HIL simulations. The power system is implemented using an OPAL-RT4512 unit, a real-time HIL simulator designed to execute and test models created with MATLAB/Simulink. The OPAL-RT4512 is particularly well suited for power system simulation applications due to its fast-processing capabilities and high precision in hardware emulation. The OPAL-RT4512 is programmed using RT-Lab software, which streamlines the implementation and testing process. The control is programmed on a dSPACE MicroLabBox unit, renowned for its compactness and versatility in enabling rapid control prototyping and algorithm testing. The OPAL-RT4512 is equipped with powerful processors and a range of I/O interfaces, facilitating integration with other power system

components. This includes the ability to interact with stability systems and real-time measurement devices, which is crucial for validating and developing advanced stability algorithms. Real-time simulation visualisation is performed using a Yokogawa DLM4038 digital storage oscilloscope designed for high-accuracy waveform analysis. This device provides a detailed observation of system signals, enhancing the analysis and validation process. It should be noted that the analogue outputs of the OPAL-RT4512 operate within a range of ± 16 V. Therefore, signals generated in the MATLAB/Simulink simulation must be appropriately scaled to ensure accurate representation on the oscilloscope.

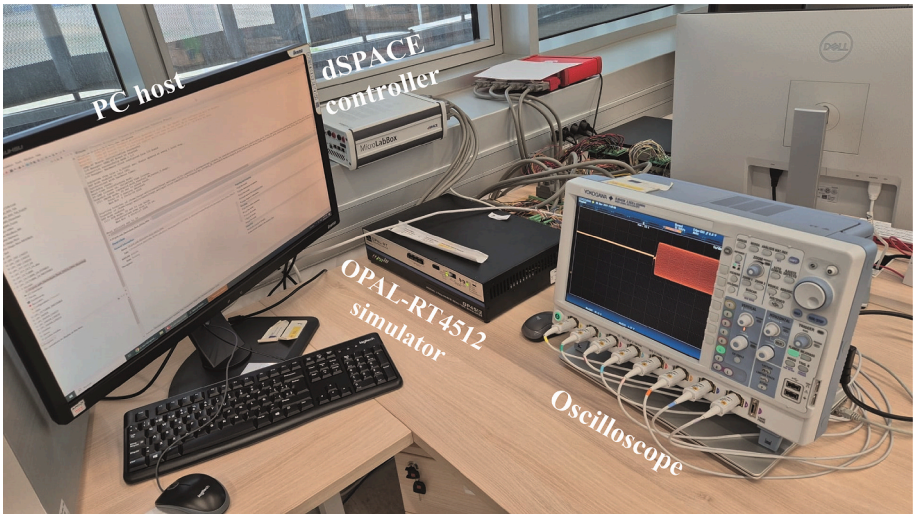

Fig. 10. Laboratory-implemented HIL experimental setup.

Data availability

Data will be made available on request.

References

[1] Xiong Y, Chen L, Zheng T, Si Y, Mei S. Electricity-Heat-hydrogen modeling of hydrogen storage system considering off-design characteristics. IEEE Access 2021; 9:156768–77.
[2] Converse AO. Seasonal energy storage in a renewable energy system,". Proc IEEE Feb 2012;100(2). pp. 401_409.
[3] Weiming L, Jiekang W, Jinjian C, Yunshou M, Shengyu C. Capacity allocation optimization framework for hydrogen integrated energy system considering hydrogen trading and long-term hydrogen storage. IEEE Access 2023;11: 15772–87.
[4] Pei W, Zhang X, Deng W, Tang C, Yao L. Review of operational control strategy for DC Microgrids with electric-hydrogen hybrid storage systems. CSEE J Power Energy Syst 2022;8(2):329–46.
[5] Trifkovic M, Sheikhzadeh M, Nigim K, Daoutidis P. Modeling and control of a renewable hybrid energy system with hydrogen storage. IEEE Trans Control Syst Tech 2014;22(1):169–79.
[6] Nehrir MH, et al. A review of hybrid Renewable/Alternative energy systems for electric power generation: configurations, control, and applications. IEEE Trans Sustain Energy 2011;2(4):392–403.
[7] Cai GW, Kong LG, Xue Y, Sun BZ. Overview of research on wind power coupled with hydrogen production technology. Auto Electric Power Syst 2014;38(21): 127–35.
[8] Agbossou K, Kolhe M, Hamelin J, Bose TK. Performance of a stand-alone renewable energy system based on energy storage as hydrogen. IEEE Trans Energy Conv 2004; 19(3):633–40.
[9] Korpas M, Holen AT. Operation planning of hydrogen storage connected to wind power operating in a power market. IEEE Trans Energy Convers 2006;21(3):742–9.
[10] Sarrias-Mena R, Fernández-Ramírez LM, García-Vazquez CA, Jurado F. Electrolyizer models for hydrogen production from wind energy systems. Int J Hydrogen Energy 2015;40(7):2927–38.
[11] Castañeda M, Cano A, Jurado F, Sánchez H, Fernández LM. Sizing optimization, dynamic modeling and energy management strategies of a stand-alone PV/ hydrogen/battery-based hybrid system. Int J Hydrogen Energy 2013;38(10): 3830–45.
[12] Valverde L, Rosa F, Bordons C. Design, planning and management of a hydrogen-based microgrid. IEEE Trans Ind Informat 2013;9(3):1398–404.
[13] Li J, Li G, Ma S, Liang Z, Li Y, Zeng W. Modeling and simulation of hydrogen energy storage system for power-to-gas and gas-to-power systems. J Mod Power Syst Clean Energy 2023;11(3):885–95.
[14] Recalde Melo DF, Chang-Chien LR. Synergistic control between hydrogen storage system and offshore wind farm for grid operation. IEEE Trans Sustain Energy 2014; 5(1):18–27.
[15] Kundur P. Power system stability and control. McGraw-Hill; 1994.
[16] Majumder R. Some Aspects of stability in microgrids. IEEE Trans on Power Systems 2013;28(3):3243–52.
[17] Farrokhabadi M, et al. Microgrid stability definitions, analysis, and examples. IEEE Trans Power Syst 2020;35(1):13–29.
[18] Kunjumuhammed LP, Pal BC, Oates C, Dyke KJ. Electrical oscillations in wind farm systems: analysis and insight based on detailed modeling. IEEE Trans Sustain Energy 2016;7(1):51–62.
[19] Harnefors L. Modeling of three-phase dynamic systems using complex transfer functions and transfer matrices. IEEE Trans Ind Electron 2007;54(4):2239–48.
[20] Sun J. Impedance-based stability criterion for grid-connected inverters. IEEE Trans Power Electron 2011;26(11):3075–8.
[21] Harnefors L, Bongiorno M, Lundberg S. Input-admittance calculation and shaping for controlled voltage-source converters. IEEE Trans Ind Electron 2007;54(6): 3323–34.
[22] Harnefors L, Wang X, Yepes AG, Blaabjerg F. Passivity-based stability assessment of grid-connected VSCs – an overview. IEEE J Emerg Select Top Power Electron 2016; 4(1):116–25.
[23] "AC side harmonics and appropriate harmonic limits for VSC HVDC," in CIGRE Reference: 754 – 2019, pp. 1-132, Feb. 2019. https://www.e-cigre.org/publications/detail/754-ac-side-harmonics-and-appropriate-harmonic-limits-for-vsc-hvdc.html.
[24] R. D. Middlebrook, Input filter considerations in design and application of switching regulators, In: Rec.1976 IEEE Ind. Appl. Soc. Annu. Meeting, pp. 366–382.
[25] Sun J. Small-signal methods for ac distributed power systems. IEEE Trans Power Electron 2009;24(11):2545–54.
[26] Zhang C, Molinas M, Rygg A, Cai X. Impedance-based analysis of interconnected power electronics systems: impedance network modeling and comparative studies of stability criteria. IEEE J Emerg Select Top Power Electron 2020;8(3):2520–33.
[27] Orellana L, Sainz L, Prieto-Araujo E, Gomis-Bellmunt O. Stability assessment for multi-infeed grid-connected VSCs modeled in the admittance matrix form. IEEE Trans Circuits Syst I Regul Pap 2021;68(9):3758–71.
[28] L. Wang, X. Xie, W. Dong, Y. Mei and A. Lei, Smallest Eigenvalues Based Logarithmic Derivative Method for Computing Dominant Oscillation Modes in Large-Scale Power Systems, J Modern Power Syst Clean Energy. https://ieeexplore.ieee.org/document/10770088.
[29] L. Wang, X. Xie, J. Shair and Y. Zhan, Logarithmic derivative based quantitative analysis of oscillatory stability in renewable powered systems, CSEE J Power Energy Syst. https://ieeexplore.ieee.org/document/10838229.
[30] Liao Y, Wang X. Impedance-based stability analysis for interconnected converter systems with open-loop RHP poles. IEEE Trans Power Electron 2020;35(4): 4388–97.
[31] Orellana L, Sainz L, Prieto-Araujo E, Cheah-Mané M, Mehrjerdi H, Gomis-Bellmunt O. Study of black-box models and participation factors for the positive-mode damping stability criterion. Int J Electr Power Energy Syst 2023;148:June.
[32] Gómez-Expósito A, Conejo AJ, Cañizares C. "Electric Energy Systems: analysis and operation," CRC Press Taylor & Francis Group. 1st Edition. Boca Raton: Taylor & Francis Group LLC; 2009.

[33] Xu W, Huang Z, Cui Y, Wang H. Harmonic resonance mode analysis. IEEE Trans Power Delivery April 2005;20(2):1182–90.
[34] O. Cartiel, L. Sainz, J. J. Mesas, and Ll. Monjo, A Damping Margin Indicator for Compensator Design by the Positive-Mode-Damping Stability Criterion, In: IEEE Trans Power Syst. https://ieeexplore.ieee.org/document/10835127.
[35] R. D. Middlebrook, and Solobodan Cuk, "Advances in Switched-Mode Power Conversion", Volumes I and II, 2nd edition, TESLAco, 1983.
[36] Ned Mohan, T.M. Undeland, W.P. Robbins, Power Electronics Converter, Application and Design, Third edition, Wiley, 2002.
[37] Forsyth AJ, Mollov SV. Modelling and control of DC-DC converters. Power Eng J 1998;12(5):229–36.
[38] Rajul Lal Gour. Small signal modelling of a buck converter using state space averaging for magnet load. Int J Recent Res Electric Electron Eng (IJRREEE) 2016; 3(3):11–7.
[39] R. H. G. Tan and M. Y. W. Teow, "A comprehensive modeling, simulation and computational implementation of buck converter using MATLAB/Simulink," In 2014 IEEE Conference on Energy Conversion (CENCON), Johor Bahru, Malaysia, pp. 37-42, 2014. https://ieeexplore.ieee.org/document/6967473.
[40] R. H. G. Tan and L. Y. H. Hoo, DC-DC converter modeling and simulation using state space approach, In: 2015 IEEE Conference on Energy Conversion (CENCON), Johor Bahru, Malaysia, pp. 42-47, 2015. https://ieeexplore.ieee.org/document/7409511.
[41] Alvarez-Ramirez J, Espinosa-Pérez G. Stability of current-mode control for DC–DC power converters. Syst Control Lett 2002;45(2):113–9.
[42] Zhang X, Wang T, Bao H, Hu Y, Bao B. Stability effect of load converter on source converter in a cascaded buck converter. IEEE Trans Power Electron 2023;38(1): 604–18.
[43] Wu HM, Pickert V, Ma MY, Ji B, Chen CM. Stability study and nonlinear analysis of DC–DC power converters with constant power loads at the fast timescale. IEEE J Emerg Sel Topics Power Electron 2020;8(4):3225–36.
[44] Jiang WT, Zhang XA, Guo FH, Chen JW, Wang P, Koh LH. Large-signal stability of interleave boost converter system with constant power load using sliding-mode control. IEEE Trans Ind Electron 2020;67(11):9450–9.
[45] El Aroudi A, Haroun R, Al-Numay M, Calvente J, Giral R. Fast-scale stability analysis of a DC-DC boost converter with a constant power load. IEEE J Emerg Sel Topics Power Electron 2021;9(1):549–58.
[46] Du WJ, Zhang JM, Zhang Y, Qian ZM. Stability criterion for cascaded system with constant power load. IEEE Trans Power Electron 2013;28(4):1843–51.
[47] Hu W, Yang R, Wang X, Zhang F. Stability Analysis of Voltage Controlled Buck Converter Feed from a Periodic Input. IEEE Trans on Ind Electron 2021;68(4): 3079–89.
[48] Sumsurooah S, Odavic M, Bozhko S, Boroyevich D. Robust stability analysis of a DC/DC buck converter under multiple parametric uncertainties. IEEE Trans Power Electron 2018;33(6):5426–41.
[49] Bélanger J, Venne P, Paquin J-N. The what, where, and why of real-time simulation. Power Energy Soc 2010.